PAPER

Check for updates

Green synthesis of polyimide by using an ethanol solvothermal method for aqueous zinc batteries†

Ya Zhao,[a] Chaoqiao Yang,[a] Hexiang Zhong, [ID] [a] Lin Li,[b] Jiangliang Hu[b] and Jiaxin Fan [ID] *[b]

Polyimides (PIs) are welcomed by battery researchers because of their exceptional heat resistance, structural design versatility, and ion-bearing capabilities. However, most of the reported PIs are synthesized by using toxic and hazardous reagents, such as ethylenediamine, p-phenylenediamine, 1-methyl-2-pyrrolidone (NMP), N,N-dimethylacetamide (DMAc), N,N-dimethylformamide (DMF), etc., which are not conducive to environmentally friendly development. In this paper, we aim at employing green solvents and raw materials to prepare PIs using a facile solvothermal method. The reactants are urea and 1,4,5,8-naphthalene tetracarboxylic acid dianhydride (NTCDA). The solvents include pure water, pure ethanol, or water–ethanol mixed solvent. The volume ratio of ethanol in the mixed solvent is regulated to obtain the optimum synthesis condition. Depending on the proportion of ethanol, the polyimide products are labeled as U-PI-0, U-PI-50, U-PI-100, etc. The polymerization degree and structure of synthesized PIs are characterized by gel permeation chromatography (GPC), X-ray diffraction (XRD), scanning electron microscopy (SEM), etc. The results indicate that U-PIs exhibit diverse morphological features, including small fragmented, strip-like, and sheet-like structures, and have relative molecular weights ranging from 7500 to 83 000. Notably, the sheet-like U-PI-100 possesses the largest specific surface area, reaching up to 4.20 m^2 g^{-1}. When employed as an electrode material in aqueous zinc batteries, U-PI-100 demonstrates superior electrochemical performance compared to others. At a charge–discharge rate of 0.05C, the initial charge/discharge capacity of U-PI-100 is measured to be 314.2/443.7 mA h g^{-1}.

1 Introduction

As human society's demand for low-carbon energy continues to grow, it is imperative to not only explore new energy sources such as solar,[1] wind[2] and geothermal energy[3] but also to address their storage challenges, so that these renewable energy sources are not hindered by seasonal variations,[4] day–night alternation, geographical environment and other factors,[5] thereby ensuring a stable and continuous supply of energy. In the field of electrochemical energy storage, lithium-ion batteries have been widely used in electronic products,[6] power batteries,[7] aerospace,[8] mining[9] and other fields. However, the low reserves of lithium in the earth limit its application in energy storage.[10] In recent years, researchers began to pay attention to other kinds of metal elements, and developed abundant ion batteries, such as K+,[11] Ca2+,[12] Mg2+,[13] and Al3+,[14] and Na–Zn[15] and Al–Zn[16] mixed ion batteries. Water-based zinc ion batteries (AZIBs) have

the advantages of low redox potential (−0.76 V), high theoretical specific capacity, being environmentally friendly and the moderate crustal abundance of zinc, which has attracted the wide attention of researchers.[17,18]

Organic polymer electrode materials are one of the hot research objects because of their low cost, strong structural design and wide ion tolerance.[19,20] PIs are a kind of organic polymer with an imide ring, which have excellent insulation, mechanical properties and heat resistance, and are widely used in microelectronics, liquid crystals, separation membranes and other fields.[21] At present, the main synthetic raw materials of PIs are dianhydride and diamine monomers, which are used to synthesize a wide variety of PI materials. PIs are a promising organic electrode material because of their simple synthesis method, stable structure and strong high electrochemical activity.[22–25] A series of PIs were synthesized as the electrode materials in batteries. Li et al.[26] selected NMP, mesitylene, and isoquinoline as solvents and combined 1,4,5,8-naphthalenetetracarboxylic dianhydride (NTH) with 4,4′,4″-(1,3,5-triazine-2,4,6-triyl) triphenylamine (TA) to successfully synthesize a novel TNP@CNT composite material in a Pyrex tube. At the current density of 20 mA g^{-1}, the first discharge and charge specific capacity of TNP@CNT were 45 mA h g^{-1} and

[a]College of Environmental and Chemical Engineering, Dalian University, Dalian, 116622, Liaoning, China

[b]School of Chemistry and Materials Engineering, Liupanshui Normal University, Liupanshui, 553004, Guizhou, China. E-mail: fmf_fjx@lpssy.edu.cn

45.8 mA h g^{-1}, respectively. Huang et al.[27] utilized the hydrogel method, employing perylene-3,4,9,10-tetracarboxylic dianhydride (PTCDA) and urea as raw materials dissolved in DMF, to synthesize three-dimensional porous PANI xerogel powder. At a current density of 0.1 A g^{-1}, the specific capacity of PUI/PANI was found to be 107 mA h g^{-1}. Wang et al.[28] dispersed PI in NMP solution and obtained the PI-Zn anode using the drop-casting method. The full battery consisting of PI-Zn and CaV$_8$O$_{20}$ exhibits excellent electrochemical performance. The PI-Zn// CaV$_8$O$_{20}$ system can retain a capacity of 306.5 mA h g^{-1} after 2000 cycles at 5 A g^{-1}.

As described above, the synthesis of polyimides (PIs) often employs organic solvents such as m-cresol,[29] 1-methyl-2-pyrrolidone (NMP),[30–32] N,N-dimethylformamide (DMF),[33] N,N-dimethylacetamide (DMAc)[34,35] and isoquinoline.[36] The use of these organic solvents is environmentally unfriendly and does not align with the objectives of green and sustainable development. The use of water as the sole solvent represents a promising approach. Currently, several studies have demonstrated the feasibility of synthesizing polyimides using water a hydrothermal method. Goujon et al.[36] synthesized a polyimide network system based on trimellitic anhydride (MTA) and 3,7-diamino-N-methylphenothiazine (MPT) using the hydrothermal method. Under the condition of C/5 rate, the initial discharge capacity of this MTA-MPT porous polyimide reached as high as 136 mA h g^{-1}. After 500 cycles at 1C rate, its capacity retention rate could still achieve 70%. Kim et al.[37] successfully prepared polyimide-based microparticles (PIMs) using hydrothermal synthesis, with benzene hexacarboxylic acid (MA) and three structurally different benzenediamine isomers (o-, m-, p-PDA) as reactants. Studies have found that the chemical composition of PIMs can be highly customized and adjusted. Yang et al.[38] synthesized two polyimide-based covalent organic frameworks, HATN-PDCOF and HATN-TAB-COF, using hexaazatrinaphthalene-2, 3,8,9,14,15-hexacarboxylic acid (HATNCA) with either p-phenylenediamine (PD) or 1,3,5-tris (4-aminophenyl) benzene (TBA). At a current density of 200 mA g^{-1}, HATN-PD-COF exhibited a discharge capacity as high as 210 mA h g^{-1}, while the HATN-TAB-COF electrode showed a discharge capacity of 150 mA h g^{-1}.

However, using water as the sole solvent may affect the polymerization of polyimide. Herein in this work, we introduced ethanol as a green solvent to prepare PIs by using a solvothermal method. A series of solvents were compared, including pure water, pure ethanol or mixed water–ethanol solvents. In mixed water–ethanol solvents, different proportions of ethanol were explored, including 0, 30%, 50%, 70%, and 100% (by volume), and the as-synthesized products were labeled as U-PI-0, U-PI-30, U-PI-50, U-PI-70 and U-PI-100. The synthesis of polyimide is displayed as Scheme 1, in which 1,4,5,8-naphthalene tetracarboxylic acid dianhydride (NTCDA) and urea were used as raw materials. The synthesized products were characterized by SEM, XRD, BET, etc. To explore electrochemical performance, batteries with PIs as the working electrode materials were assembled, with a zinc counter electrode, and 1.0 mol L^{-1} ZnSO$_4$ electrolyte. The electrochemical performance was investigated by CV, EIS, GCD, etc.

Scheme 1 Synthesis of polyimide.

2 Experiment

2.1 Materials and reagents

The materials and reagents are listed in Table 1.

2.2 Synthesis of U-PIs

PIs were synthesized by a solvothermal method. Water or ethanol was used as the solvent. For urea was used as reactant, the products were labeled as U-PI. Based on the volume proportion of ethanol in the solvent, the polyimide products were labeled as U-PI-0, U-PI-30, U-PI-50, U-PI-70, U-PI-100. First, 0.1 mol naphthalic anhydride was dispersed in absolute ethanol (A), 0.2 mol urea was dissolved in distilled water or ethanol (B), and then A was dripped into B by disposable dropper, which was then transferred to a constant temperature magnetic heating stirrer for heating and stirring at 80 °C and 1500 rpm for 3 hours. Second, the mixed solution was transferred to a 150 mL reaction kettle, and the reaction was kept at 200 °C for 24 hours. Third, the obtained product was centrifuged at 9000 rpm for 5 times. Finally, product was dried at 80 °C for 10 h, and then ground into powder by agate mortar.

2.3 Material characterization

Fourier transform infrared (FTIR) spectroscopy was conducted in transmission mode on an infrared spectrometer (FTIR, Nicolet iS5 type) with a wavenumber range of 4000 to 400 cm^{-1}. The crystalline structure of the synthetic material was analyzed by X-ray diffraction (XRD) using a Rigaku MiniFlex 600 X-ray diffractometer. The scanning speed was 5° min^{-1} from 10° to 80°. The morphology and structure were characterized using a scanning electron microscope (ZEISS Gemini SEM 300). The water content of the sample was determined using a thermogravimetric analyzer (TG, Mettler TGA2) under an air atmosphere with a heating rate of 10 °C min^{-1} and a temperature range of 30–800 °C. The specific surface area and porosity of the sample were measured using a fully automatic surface area and porosity analyzer (BET, Micromeritics ASAP 2460) under nitrogen at 120 °C. The degree of polymerization was tested using gel permeation chromatography (GPC, Agilent PL-GPC50). To determine the content of organic elements, an organic elemental analyzer (EA, Elementar Vario EL cube) is employed.

Table 1 Materials and reagents

Material	Supplier	Purity/thickness
Urea	Anhui Zesheng Technology co., Ltd	99%
1,4,5,8-Naphthalene tetracarboxylic acid dianhydride(NTCDA)	Anhui Zesheng Technology co., Ltd	96%
Anhydrous ethanol	Tianjin Fuyu Fine co., Ltd	Analytically pure
$ZnSO_4$	Chengdu Jinshan chemical reagent Company	99.5%
Zinc foil	Afaisha	99.99%/0.02 mm

2.4 Electrochemical testing

The electrode material was prepared by mixing the active material, acetylene black, and polytetrafluoroethylene in a mass ratio of 8 : 1 : 1. The uniformly mixed slurry was then coated onto a carbon foil current collector, dried at 80 °C for 12 hours, and cut into 14 mm circle disks for subsequent use. The mass loading of the active material was approximately 0.9–1 mg cm^{-2}. Harf cells were assembled, where U-PI was used as the working electrode, with a Zn metal counter electrode, and glass fiber membrane separator. 1 M $ZnSO_4$ solution was prepared as electrolyte. A coin-cell battery (CR2025) was then fabricated. Cyclic voltammetry (CV) and electrochemical impedance spectroscopy (EIS) tests were conducted on the Versa STAT 3 electrochemical workstation. The voltage range for the CV test was set from 0 to 1.7 V. For the EIS test, the frequency range spanned from 100 000 Hz to 0.01 Hz, with a potential amplitude of 5 mV. The battery's specific capability, cycling performance, and galvanostatic charge–discharge (GCD) performance were tested on the Land 3002 A battery testing system within a voltage range of 0 to 1 V. In the GCD process, the battery was first discharged to 0 V, then charged to 1 V, and this cycle was repeated.

3 Results and discussion

3.1 Products characterization

Fig. S1† depicts the solubility of 30 mg of NTCDA monomer and 30 mg of U-PI in 5 mL of NMP solvent. The NTCDA monomer is fully soluble in the NMP solvent, whereas U-PIs cannot be dissolved in NMP, indicating successful polymerization. Table 2 lists the yields of U-PIs, with the yields above 70%.

To investigate the bonding structure features of U-PI in depth, Fourier transform infrared spectroscopy (FTIR) tests were conducted. As shown in Fig. 1a and S2,† the test results indicate that the spectral curves of U-PI almost overlap at different water–ethanol ratios, demonstrating a high degree of similarity in their molecular structures. Specifically, peaks observed at 1755 cm^{-1} and 1715 cm^{-1} correspond to the asymmetric (v_{as}) and symmetric (v_s) stretching vibrations of

C=O in 1,4,5,8-naphthalenetetracarboxylic dianhydride monomer, respectively. Peaks at 1705 cm^{-1}, 1675 cm^{-1}, and 765 cm^{-1} originate from the asymmetric stretching (v_{as}), symmetric stretching (v_s), and bending vibrations (δ) of C=O in the imide group. Additionally, peaks at 1345 cm^{-1} and 1575 cm^{-1} reflect the characteristic absorptions of naphthalene and C–N. The simultaneous appearance of these absorption peaks further confirms the successful synthesis of U-PI. Furthermore, absorption peak at 1777 cm^{-1}, attributed to the C=O in urea, was observed.[39–46] Meanwhile, N–H absorption peaks of urea were observed in the range of 3200–3600 cm^{-1}.[43] Notably, when the ethanol content was 10%, 30%, 50%, and 70%, no clear absorption peak of urea C=O was detected in the FTIR spectra of the synthesized U-PI. However, when the ethanol content increased to 100%, the C=O absorption peak of urea emerged, indicating that U-PI synthesized under higher ethanol content conditions exhibited a higher degree of amide formation compared to U-PI-0, U-PI-30, U-PI-50, and U-PI-70 electrode materials.

Fig. 1b shows the X-Ray Diffraction (XRD) spectra of urea, NTCDA, and U-PI-0. From the figure, we can observe strong diffraction peaks for Urea and NTCDA. This is mainly due to the p–π conjugation effect between the unshared electron pairs on the two nitrogen atoms in urea and the carbon-based π electrons, as well as the π–π stacking interactions between NTCDA molecules. However, compared to urea and NTCDA, the intensity of the diffraction peaks of U-PI has decreased, implying that the crystal structure and degree of crystallinity of U-PI have undergone certain changes. Fig. S3† presents the XRD spectra of U-PI-30, U-PI-50, U-PI-70, and U-PI-100. By observation, it can be noted that these U-PI materials exhibit similar diffraction peak characteristics. Specifically, the diffraction peak intensity of U-PI-100 is relatively low, further indicating its lower crystallinity.[46,47] To further confirm the composition of U-PI, an organic elemental analyzer (EA) was used, and the results are shown in Table S1.† The contents of C, N, H, O are 63.048%, 9.594%, 2.665%, 24.182%, respectively.

Table 2 Yields of U-PIs

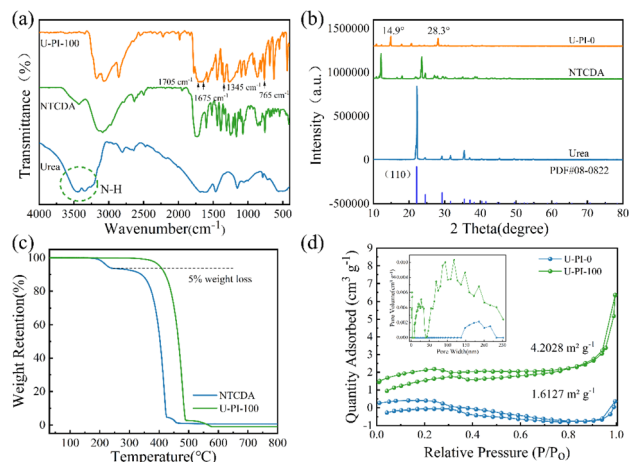|	U-PI-0	U-PI-30	U-PI-50	U-PI-70	U-PI-100
NTCDA reactant weights (g)	2.6824	2.6822	2.6822	2.6820	2.6823
Calculated U-PIs weights (g)	2.9206	2.9204	2.9204	2.9202	2.9205
Actual product weight (g)	2.1368	2.2056	2.1908	2.2149	2.2229
Yields	73.16%	75.52%	75.02%	75.84%	76.11%

Fig. 1 Characterization of materials: (a) FTIR spectrums; (b) XRD patterns; (c) TG curves; (d) BET plots (the insets show the corresponding pore size distribution).

Fig. 1c presents the Thermogravimetry (TG) curves of NTCDA and U-PI-100 from 30 °C to 800 °C under an N_2 atmosphere. NTCDA experiences a 5% weight loss between 180 °C and 240 °C due to the decomposition of carbonyl groups, whereas U-PI-100 remains stable until decomposition begins at 320.1 °C. Similarly, U-PI-0, U-PI-30, U-PI-50, and U-PI-70 (Fig. S4†) all exhibit stability below 320 °C, demonstrating the excellent thermal stability of the U-PI materials. Fig. 1d showcases the N_2 adsorption/desorption isotherms of U-PI-0 and U-PI-100 and the corresponding pore size distribution. The adsorption/desorption curves of the U-PI materials exhibit similar trends, with U-PI-0 and U-PI-100 possessing specific surface areas of 4.2028 m^2 g^{-1} and 1.6127 m^2 g^{-1}, respectively. The specific surface areas of U-PI-30, U-PI-50, and U-PI-70 are 2.7815 m^2 g^{-1}, 3.6379 m^2 g^{-1}, and 3.0619 m^2 g^{-1}, separately (Fig. S5†). Fig. S6† depicts the pore size distributions corresponding to U-PI-0 and U-PI-100. U-PI-0 exhibits predominantly macropores ranging from 136 to 234 nm, while U-PI-100 is a porous material. Likewise, U-PI-30, U-PI-50, and U-PI-70 are also porous materials with pore sizes distributed between 0 and 250 nm (Fig. S7†). The high specific surface area and pore volume of U-PI-100 facilitate ion diffusion, expose more carbonyl groups, and provide a greater number of active sites.
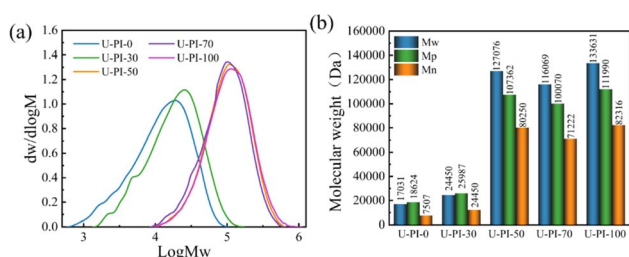
Fig. 2a describes the Gel Permeation Chromatography (GPC) charts of U-PI-0, U-PI-30, U-PI-50, U-PI-70, and U-PI-100. U-PI-0 and U-PI-30 exhibit a wide range of molecular weights and relatively small molecular weights, while U-PI-50, U-PI-70, and U-PI-100 display narrower molecular weight ranges and larger molecular weights. Fig. 2b illustrates the bar chart the weight-average molecular weight (M_w), M_p (it refers to the molecular weight at the highest peak in the distribution curve), and number-average molecular weight (M_n) values of U-PI-0, U-PI-30, U-PI-50, U-PI-70, and U-PI-100. U-PI-100 exhibits superior molecular weight characteristics compared to the other U-PI materials.

Fig. 3a–f provide detailed information on the surface morphologies of NTCDA, U-PI-50 and U-PI-100. Fig. 3a and d clearly show the delicate dune-like structure of the NTCDA surface, with evenly distributed pores observable upon magnification. In contrast, Fig. 3b and e reveal that U-PI-50 is composed of tightly packed small fragments with almost no gaps. Fig. 3c and f, on the other hand, indicate that U-PI-100 exhibits a flaky morphology, with a granular texture visible on its surface under magnification. Furthermore, both U-PI-0 and U-PI-30 exhibit dense crystalline structures. Upon closer inspection, the surface of U-PI-0 exhibits only subtle undulations or minute irregularities, whereas U-PI-30 is more pronounced. Additionally, U-PI-70 is composed of strip-like structures, as shown in Fig. S8.† Compared to NTCDA, the morphologies of U-PI materials have undergone significant changes. The small fragmentary and flaky morphologies possess a larger specific surface area, which is beneficial for their performance in practical applications.

Fig. 4 appears the EDS spectra of U-PI-50, U-PI-70, and U-PI-100. Meanwhile, Fig. S9† provides the EDS spectra of U-PI-0 and U-PI-30. Through EDS mapping analysis, we can confirm the presence of C, N, and O elements in U-PI materials, and their distribution within the materials is relatively uniform.

3.2 Electrochemical performance

3.2.1 Electrochemical properties of U-PIs.
Fig. 5a shows the EIS results of NTCDA, U-PI-50, and U-PI-100. The electrochemical charge transfer impedance (R_{ct}) corresponds to the semicircle in the mid-to-high frequency region of the Nyquist plot. The slope impedance in the low-frequency region, known

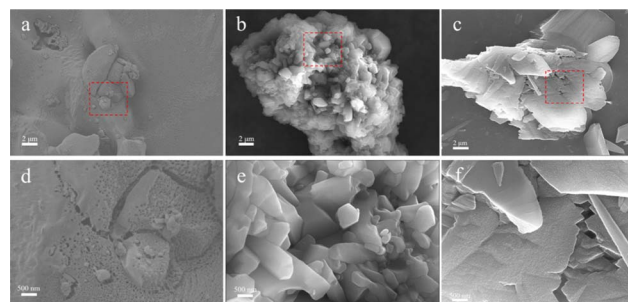Fig. 2 (a) GPC chromatograms of U-PIs; (b) the M_w, M_p, and M_n values of U-PIs.

Fig. 3 SEM image: (a) NTCDA; (b) U-PI-50; (c) U-PI-100; (d–f) corresponding magnified SEM images.
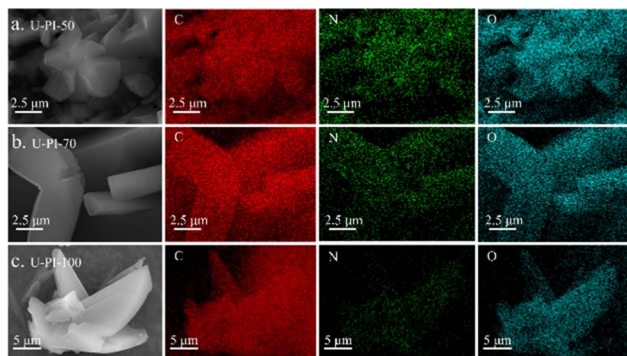
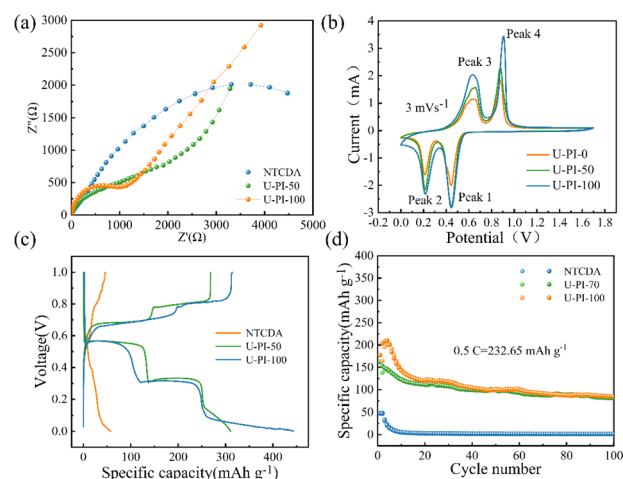Fig. 4 EDS mapping of (a) U-PI-50, (b) U-PI-70, and (c) U-PI-100.

Fig. 5 Electrochemical performances: (a) Nyquist plots; (b) CV curves at a scan rate of 3 mV s^{-1}; (c) the first charge–discharge curve at 0.05C; (d) cycling performance 0.5C.

as Warburg impedance (Z_w). The ohmic impedance (R_s) of U-PI is similar across samples. The obtained data were fitted using ZSimpWin 3.60. The R_{ct} values for NTCDA, U-PI-50, and U-PI-100 are 4504 Ω, 950.8 Ω, and 948.5 Ω, respectively. For U-PI-0, U-PI-30, and U-PI-70, the R_{ct} values are 1692 Ω, 984 Ω, and 1223 Ω, respectively (Fig. S10†). The R_{ct} of U-PI is improved compared to NTCDA, and the ethanol content has an impact on U-PI, with a decrease in R_{ct} favoring charge transfer in U-PI.

Fig. 5b presents the cyclic voltammetry (CV) curves of U-PI-0, U-PI-50, and U-PI-100 at a scan rate of 3 mV s^{-1} and a voltage range of 0–1.7 V. As observed from the CV curves, two pairs of redox peaks emerge near 0.44/0.88 V and 0.21/0.65 V for U-PI-0, 0.44/0.88 V and 0.21/0.66 V for U-PI-50, and 0.45/0.91 V and 0.22/0.63 V for U-PI-100, respectively. The positions of these peaks undergo minor changes, whereas their intensities vary significantly, with U-PI-100 exhibiting the highest intensity. These peaks correspond to the reversible transformation of carbonyl groups during the insertion/extraction of Zn^{2+}, occurring as a two-step process.[48,49] Additionally, the CV curve of the NTCDA monomer exhibits a spindle shape without redox peaks

(Fig. S14†). Both U-PI-30 and U-PI-70 also exhibit two pairs of redox peaks (Fig. S11†).

Fig. 5c displays the charge–discharge curves at a rate of 0.05C. It can be observed that the charge–discharge platforms of the NTCDA monomer are not distinct, while both U-PI-50 and U-PI-100 reversible two charge–discharge platforms, including a low discharge platform below approximately 0.1 V. Similar patterns are observed for U-PI-0, U-PI-30, and U-PI-70 (Fig. S12†). The two charge–discharge platforms correspond to the two pairs of redox peaks in the CV curve shown in Fig. 5b. The low discharge platform below 0.1 V is likely to be caused by the pseudocapacitance process, which appears in the first cycle, and gradually disappears in the subsequent cycles.[50–53]

Among the materials tested, NTCDA, U-PI-0, U-PI-30, U-PI-50, U-PI-70, and U-PI-100 exhibited maximum charge–discharge capacities of 45.8/57.7 mA h g^{-1}, 100.9/139.4 mA h g^{-1}, 144.9/175.6 mA h g^{-1}, 268.5/310.8 mA h g^{-1}, 194.7/238.8 mA h g^{-1}, and 314.2/443.7 mA h g^{-1}, respectively. Fig. S15† demonstrates the reduction reactions of U-PI-100 during the initial discharge process. It is possible that Zn^{2+} initially reacts with the carbonyl group from urea at ~0.55 V, and subsequently associates with the carbonyl group from the naphthalene monomer at ~0.3 V.[48,54] Meanwhile, the sloping platform below 0.1 V belongs to the pseudocapacitance process.[48,54] Overall, the performance of U-PIs surpasses that of NTCDA, with U-PI-100 exhibiting the best performance. This is attributed to the large specific surface area and pore volume of U-PI-100, which exposes more carbonyl groups and thereby enhances the maximum charge–discharge specific capacity of U-PI-100.

Fig. 5d demonstrates the cycling performance of NTCDA, U-PI-70, and U-PI-100. As can be seen from the figure, all three materials require an activation process. The cycling performance of the NTCDA monomer is significantly lower than that of U-PI-70 and U-PI-100. Furthermore, the cycling performance of U-PI-0, U-PI-30, and U-PI-50 is also superior to that of the NTCDA monomer (Fig. S13†). Based on these findings, we have conducted a detailed investigation on U-PI-100.

3.2.2 The electrochemical properties of U-PI-100. Fig. 6a presents the charge–discharge curves of the first cycle at different rates. As can be seen from the figure, as the rate increases from 0.05C to 1C, the polarization effect becomes more pronounced, leading to a gradual decrease in charge–discharge capacity. As shown in Table S2,† a comparison is made between the U-PI-100 and other polyimides in terms of the diamine materials used, solvents, and electrochemical performance. The synthesis of U-PI-100, which utilizes urea as the raw material and ethanol as the solvent, represents an environmentally friendly synthetic technique. Furthermore, the U-PI-100 exhibits a superior initial charge and discharge capacity compared with other PIs.

Fig. 6b compares the cycling performance of the U-PI-100 electrode at a rate of 1C for the first 200 cycles. The initial charge capacities are 82.9 and 91.9 mA h g^{-1}, respectively. The coulombic efficiency exceeds 100% in the first few cycles, possibly due to instability in the initial state of the battery. However, in subsequent cycles, the charge–discharge capacity
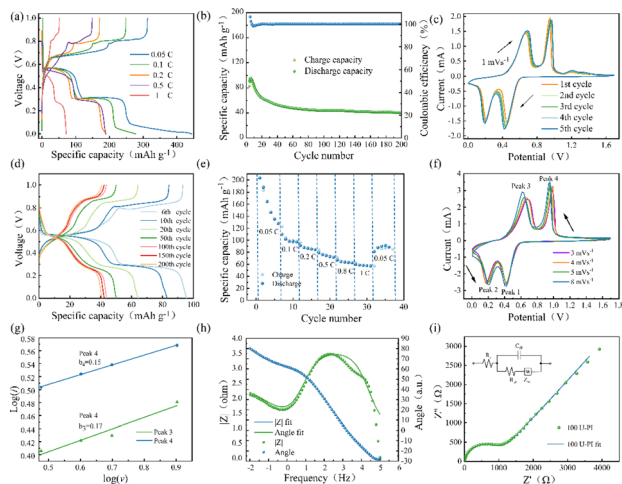
Fig. 6 Electrochemical performances of U-PI-100: (a) GCD curves at different rates; (b) cycling performance at a rate of 1C; (c) CV curve at a scan rate of 1 mV s^{-1} (0–1.7 V); (d) GCD curves at different cycles under a rate of 1C; (e) rate performance from 0.05C to 1C; (f) CV curves at different scan rates; (g) linear fitting diagram of log(i) and log(v) obtained from the CV curves; (h) Nyquist plot; (i) Bode plot.

remains stable and consistent, with the coulombic efficiency maintained at around 100%. Fig. 6c shows the CV curves of the U-PI-100 electrode material for the first five cycles, with a potential window of 0–1.7 V and a scan rate of 1 mV s^{-1}. The CV curves of the U-PI-100 electrode almost overlap, indicating reversibility. Additionally, there are two pairs of redox peaks at 0.44 V/0.97 V and 0.19 V/0.68 V, corresponding to the zinc insertion/extraction behavior of carbonyl groups, indicating that the U-PI-100 electrode material involves a two-electron transfer reaction. Two weak oxidation peaks are observed at 1.19 V and 1.34 V, suggesting that the carbonyl group derived from urea may also be involved in the reaction.

Fig. 6d presents the charge/discharge curves of the U-PI-100 electrode at various cycles (6th, 10th, 20th, 50th, 100th, 150th, and 200th) within a voltage range of 0–1 V and at a rate of 1C. The specific discharge capacities are 96.5, 82.8, 64, 49.7, 43.8, 42.2, and 40.5 mA h g^{-1}, respectively. From the 100th to the 200th cycle, the specific discharge capacity decreases by 3.3 mA h g^{-1}, indicating good capacity retention. Additionally, voltage plateaus appear around 0.56 V and 0.31 V in the charge/discharge curves, which gradually narrow in subsequent cycles. This could be due to changes in the layered structure of U-PI-100, hindering the insertion/extraction behavior of Zn^{2+}. Fig. 6e illustrates the rate performance of the U-PI-100 electrode. As the rate increases from 0.05C to 1C, the specific charge/discharge capacities gradually decrease.

Fig. 6f displays the CV curves at scan rates of 3, 4, 5, and 8 mV s^{-1}. With increasing scan rates, the redox peak intensities gradually increase, and the oxidation peaks shift to the left while the reduction peaks shift to the right. The measured peak current (i) and scan rate (v) exhibit the following relationship:[55,56]

$$i = av^b \quad (1)$$

$$\log(i) = \log(a) + b \log(v) \quad (2)$$

Using eqn (2), the b-values for Peak 3 and Peak 4 were calculated, where the peak current is denoted as i and the scan rate is v. The b-value ranges from 0.5 to 1, with 0.5 indicating a diffusion-controlled process and 1 indicating a capacitance-controlled process. If the b-value falls between 0.5 and 1, it suggests that the process is controlled by both mechanisms. The fitted lines for U-PI-100 are shown in Fig. 6g. Through mathematical fitting, the b-values for the two oxidation peaks, Peak 3 and Peak 4, were found to be 0.15 and 0.17, respectively, indicating that the diffusion-controlled behavior dominates in the non-porous U-PI-100 electrode. Fig. 6h and i present the Nyquist plot and Bode plot of an uncycled U-PI-100, respectively. From these plots, it can be observed that there is a small fitting error, and the circuit model is represented as the Warburg–Randles combined equivalent circuit $[R(Q(RW))]$.[42,57,58] In this model, R_s represents the solution resistance, C_{dl} represents the double-layer capacitance, R_{ct} represents the charge transfer resistance, and R_p represents the polarization resistance. In the Warburg–Randles equivalent circuit model, R_p, R_{ct}, and C_{dl} jointly influence the impedance curve of the electrochemical reaction. At higher frequencies, these three components form a semicircle, while at lower frequencies, the Warburg impedance (Z_w) corresponds to a line with a slope of approximately 45°.

4 Conclusions

In summary, a series of polyimides, including U-PI-0, U-PI-30, U-PI-50, U-PI-70, and U-PI-100, were successfully synthesized through solvothermal method in water or ethanol solvents. The U-PIs exhibit superior thermal stability and various morphological characteristics. Different ethanol content leads to distinct morphologies, with U-PI-50 presenting as small fragmented pieces, U-PI-70 as strip-like structures, and U-PI-100 as sheet-like structures. Among the U-PIs, U-PI-100 exhibits better initial charge–discharge performance, improved cycling performance and rate capability. Notably, U-PI-100 possesses a higher pore volume and larger specific surface area, making it more effective in carrying metal ions. Furthermore, the use ethanol as solvent is much more environmentally friendly and cost-effective, compared with the organic solvent methods, providing a greener option for the synthesis of polyimide electrode materials.

Author contributions

Ya Zhao conducted the experiment, data analysis and collation, and wrote the manuscript, Chaoqiao Yang and Jiangliang Hu guided the experiment, Hexiang Zhong provided technical guidance, Lin Li commanded the operation of the experimental instruments, and Jiaxin Fan revised the first draft and provided financial support.

Conflicts of interest

The authors declare that there is no conflict of interest regarding the publication of this paper.

Acknowledgements

Notes and references

1 M. Pastore, S. Caramori and P. C. Gros, *Acc. Chem. Res.*, 2024, **57**, 439–449.

2 H. Balta and Z. Yumurtaci, *Energies*, 2024, **17**, 603.

3 R. S. Anand, A. Li, W. Huang, J. Chen, Z. Li, Q. Ma and F. Jiang, *Renewable Sustainable Energy Rev.*, 2024, **193**, 114286.

4 K. VankadaraS. B. Daram, *Multimedia Tools and Applications*, 2024, vol. 24, pp.1-26.

5 X. Zhou, Y. Xu and F. Zhang, *Int. J. Heat Mass Transfer*, 2017, **115**, 398–405.

6 S. Wang, T. Cheng, Y. Z. Zhang, X. Wu, S. Xiao and W.-Y. Lai, *Appl. Phys. Rev.*, 2022, **9**, 041310.

7 C. Wett, J. Lampe, J. Haß, T. Seeger and B. Turan, *Batteries*, 2024, **10**, 57.

8 C. Chen, J. Wei and Z. Li, *Processes*, 2023, **11**, 2333.

9 L. Meng, G. Wang, K. W. See, Y. Wang, Y. Zhang, C. Zang, R. Zhou and B. Xie, *Energies*, 2022, **15**, 3884.

10 Q. Yang, H. Li, C. Feng, Q. Ma, L. Zhang, R. Wang, J. Liu, S. Zhang, T. Zhou, Z. Guo and C. Zhang, *Nanoscale*, 2022, **14**, 5814–5823.

11 X. He, N. Iqbal, U. Ghani and T. Li, *J. Alloys Compd.*, 2024, **981**, 173680.

12 T. Fu, Y. Feng, W. Gao and X. Li, *J. Mol. Model.*, 2024, **30**, 34.

13 M. Javed, A. Shah, J. Nisar, S. Shahzad, A. Haleem and I. Shah, *ACS Omega*, 2024, **9**, 4229–4245.

14 Y. Wang, Z. Zhang, F. Yuan and B. Wang, *J. Power Sources*, 2024, **597**, 234110.

15 C. Yang, S. Ding, Y. Zhao, J. Zhou, L. Li and J. Fan, *Dalton Trans.*, 2023, **52**, 16984–16992.

16 C. Lu, Z. Wang, J. Gao, J. Li and L. Wei, *Adv. Energy Mater.*, 2024, 2304016.

17 Y. Cui, Z. Ju, R. Yu, H. Du, B. Zhang, Y. Wang and G. Yu, *ACS Mater. Lett.*, 2024, **6**, 611–626.

18 B.-R. Xu, Q.-A. Li, Y. Liu, G.-B. Wang, Z.-H. Zhang and F.-Z. Ren, *Rare Met.*, 2024, **43**, 1599–1609.

19 S. Muench, A. Wild, C. Friebe, B. Häupler, T. Janoschka and U. S. Schubert, *Chem. Rev.*, 2016, **116**, 9438–9484.

20 Y. Tong, Y. Wei, A. Song, Y. Ma and J. Yang, *ChemSusChem*, 2023, e202301468.

21 P. Ma, C. Dai, H. Wang, Z. Li, H. Liu, W. Li and C. Yang, *Compos. Commun.*, 2019, **16**, 84–93.

22 M. Mehrabi and V. Vatanpour, *Mater. Today Chem.*, 2024, **35**, 101895.

23 A. Nimkar, G. Bergman, E. Ballas, N. Tubul, N. Levi, F. Malchik, I. Kukurayeve, M. S. Chae, D. Sharon, M. Levi, N. Shpigel, G. Wang and D. Aurbach, *Angew. Chem., Int. Ed.*, 2023, **62**, e202306904.

24 Y. Song, L. Yuan, Z. Wang and S. Yang, *Polym. Adv. Technol.*, 2019, **30**, 1243–1250.

25 F. Windrich, E. J. Kappert, M. Malanin, K.-J. Eichhorn, L. Häussler, N. E. Benes and B. Voit, *Eur. Polym. J.*, 2016, **84**, 279–291.

26 K. Li and H.-G. Wang, *J. Phys.: Conf. Ser.*, 2021, **2085**, 012032.

27 H. Huang, K. Wu, R. Ma, J. Huang, X. Zhang, L. Li, Y. Liu and C. Xiong, *Adv. Powder Technol.*, 2022, **33**, 103878.

28 L. Wang, X. Wang, B. Song, Z. Wang and F. Wan, *Energy Technol.*, 2022, **11**, 2201084.

29 J. Wang, H. Liu, C. Du, X. Zhang, Y. Liu, H. Yao, Z. Sun and S. Guan, *Chem. Eng. J.*, 2022, **444**, 136598.

30 Y.-C. Wu, G.-T. Huang, M.-Y. Lian, R. Liang, H.-L. Deng, F. Gan, Y.-F. Zhang, N.-B. Yi, L.-Y. Tian, C.-P. Ma and Y. Wei, *Chin. J. Polym. Sci.*, 2023, **41**, 1609–1616.

31 J. Zhang, X. Lai, J. Li, T. Wang, L. Shan, F. Niu, G. Zhang and R. Sun, *Polym. Compos.*, 2023, **44**, 5058–5069.

32 S. Zhang, K. Zhu, Y. Gao, T. Bao, H. Wu and D. Cao, *Chem.–Asian J.*, 2023, **18**, e202300439.

33 Q. Wang, J. Shi, X. Zhang, L. Weng, S. Yan, Y. Wu and C. Li, *J. Mater. Sci.: Mater. Electron.*, 2024, **35**, 300.

34 H. Dong, J. Dong, X. Li, X. Zhao, Q. Xu, J. Zhang and Q. Zhang, *ACS Appl. Polym. Mater.*, 2024, **6**, 2371–2380.

35 H. Jeon, C. Na, L. K. Kwac, H. G. Kim and J.-H. Chang, *Sci. Rep.*, 2024, **14**, 655.

36 N. Goujon, M. Lahnsteiner, D. A. Cerron-Infantes, H. M. Moura, D. Mantione, M. M. Unterlass and D. Mecerreyes, *Mater. Horiz.*, 2023, **10**, 967–976.

37 T. Kim, B. Park, K. M. Lee, S. H. Joo, M. S. Kang, W. C. Yoo, S. K. Kwak and B. S. Kim, *ACS Macro Lett.*, 2018, **7**, 1480–1485.

38 X. Yang, L. Gong, Z. Liu, Q. Zhi, B. Yu, X. Chen, K. Wang, X. Li, D. Qi and J. Jiang, *Sci. China: Chem.*, 2024, **67**, 100–1310.

39 L. Chen, Y. Li, X. Wang, J. Wu, Y. Ding, S.-B. Ren, L. Zhang, Z. Xu, B. Chen, D.-M. Han and Y.-p. Wu, *Chem. Eng. J.*, 2023, **464**, 142658.

40 A. Nimkar, B. Gavriel, G. Bergman, M. Turgeman, T. Fan, N. Shpigel and D. Aurbach, *ACS Sustain. Chem. Eng.*, 2023, **11**, 1428–1433.

41 P. Xu, F. Gao and D. Liu, *Adv. Mater. Interfaces*, 2023, **10**, 2300464.

42 A. Li, Z. Rong, B. Yuan, F. Cheng and W. Zhang, *ACS Appl. Energy Mater.*, 2023, **6**, 1862–1870.

43 W. Zhang, Q. Wu, W. Shao, F. Li, H. Chen, Y. Pei and J. Wang, *Polym. Chem.*, 2023, **14**, 4188–4198.

44 Y. Liu, Y. Lu, A. Hossain Khan, G. Wang, Y. Wang, A. Morag, Z. Wang, G. Chen, S. Huang, N. Chandrasekhar, D. Sabaghi, D. Li, P. Zhang, D. Ma, E. Brunner, M. Yu and X. Feng, *Angew Chem. Int. Ed. Engl.*, 2023, **62**, e202306091.

45 Q. Zhao, R. R. Gaddam, D. Yang, E. Strounina, A. K. Whittaker and X. S. Zhao, *Electrochim. Acta*, 2018, **265**, 702–708.

46 W. Han, M. Li, Y. Ma and J. Yang, *Electrochim. Acta*, 2022, **403**, 139550.

47 C. Wang, R. Chu, Z. Guan, Z. Ullah, H. Song, Y. Zhang, C. Yu, L. Zhao, Q. Li and L. Liu, *Nanoscale*, 2020, **12**, 4729–4735.

48 C. Chen, X. Zhao, H.-B. Li, F. Gan, J. Zhang, J. Dong and Q. Zhang, *Electrochim. Acta*, 2017, **229**, 387–395.

49 Y. Wang, Z. Liu, C. Wang, Y. Hu, H. Lin, W. Kong, J. Ma and Z. Jin, *Energy Storage Mater.*, 2020, **26**, 494–502.

50 Y. Zhang, W. Fan, H. Lu and T. Liu, *Electrochim. Acta*, 2018, **283**, 1763–1772.

51 F. Ji, S. Gou, J. Tang, Y. Xu, S. M. Eldin, W. Mai, J. Li and B.-T. Liu, *Chem. Eng. J.*, 2023, **474**, 145786.

52 X.-W. Huang, S.-Y. Liao, Y.-Z. Li, C.-S. Liu, W.-X. Cheng, C. Zhao, Y.-Z. Chen, Y.-D. Liu and Y.-G. Min, *J. Alloys Compd.*, 2022, **919**, 165559.

53 Q. Zhao, D. Yang, A. K. Whittaker and X. S. Zhao, *J. Power Sources*, 2018, **396**, 12–18.

54 L. Yao, C. Ma, L. Sun, D. Zhang, Y. Chen, E. Jin, X. Song, Z. Liang and K. X. Wang, *J. Am. Chem. Soc.*, 2022, **144**, 23534–23542.

55 S. Zheng, L. Miao, T. Sun, L. Li, T. Ma, J. Bao, Z. Tao and J. Chen, *J. Mater. Chem. A*, 2021, **9**, 2700–2705.

56 L. Zhao, J. Yu, C. Xing, Z. Ullah, C. Yu, S. Zhu, M. Chen, W. Li, Q. Li and L. Liu, *Energy Storage Mater.*, 2019, **22**, 433–440.

57 Q. Zhang, Y. Xu, N. Lv, H. Li, Z. Wei, T. Tian, Y. Wang and H. Tang, *Electrochim. Acta*, 2023, **461**, 142638.

58 J. Wang, H. Yao, C. Du and S. Guan, *J. Power Sources*, 2021, **482**, 228931.